Volume 1 | Number 1 | Jan 2013 | Pages 1–100

Journal of
Materials Chemistry A

Materials for energy and sustainability
www.rsc.org/materialsA

Li⁺

ROYAL SOCIETY
OF CHEMISTRY

ROYAL SOCIETY
OF CHEMISTRY

www.rsc.org/materialsA

Enhanced Thermoelectric Properties of $Sr_5In_2Sb_6$ via Zn-doping

Sevan Chanakian[1], Alex Zevalkink[1,2], Umut Aydemir[1], Zachary M. Gibbs[3], Gregory Pomrehn[1], Jean-Pierre Fleurial[2], Sabah Bux[2], G. Jeffrey Snyder[1]

[1] Department of Applied Physics and Materials Science, California Institute of Technology, 1200 E California Blvd, Pasadena, USA

[2] Thermal Energy Conversion Technologies Group, Jet Propulsion Laboratory, 4800 Oak Grove Drive, Pasadena, USA

[3] Division of Chemistry and Chemical Engineering, California Institute of Technology, 1200 E California Blvd, Pasadena, USA

Abstract

Zintl phases exhibit inherently low thermal conductivity and adjustable electronic properties, which are integral to designing high-efficiency thermoelectric materials. Inspired by the promising thermoelectric figure of merit of optimized $A_5M_2Sb_6$ Zintl phases (A = Ca or Sr, M = Al, Ga, In), Zn-doped $Sr_5In_{2-x}Zn_xSb_6$ (x = 0, 0.025, 0.05, 0.1) compounds were investigated. Optical absorption measurements combined with band structure calculations indicate two distinct energy transitions for $Sr_5In_2Sb_6$, one direct ($E_g \sim 0.3$ eV) and the other from a lower valence band manifold to the conduction band edge ($E_g \sim 0.55$ eV). $Sr_5In_2Sb_6$ exhibits nondegenerate p-type semiconducting behavior with low carrier concentration ($\sim 4 \times 10^{18}$ h$^+$/cm^3 at 300 K). Charge carrier tuning was achieved by Zn^{2+} substitution on the In^{3+} site, increasing carrier concentrations to up to 10^{20} h$^+$/cm^3. All samples displayed relatively low thermal conductivities (~ 0.7 W/m-K at 700 K). The Zn-doped samples exhibited significantly higher zT values compared to the undoped sample, reaching a value of ~ 0.4 at 750 K for $Sr_5In_{1.9}Zn_{0.1}Sb_6$.

Introduction

Thermoelectric devices produce electricity when a heat gradient is applied, making them an attractive means to convert waste heat into usable energy [1-3]. The maximum efficiency of thermoelectric materials is determined by the dimensionless thermoelectric figure of merit, $zT = \alpha^2 T/\rho\kappa$, where α is the Seebeck coefficient, ρ is the electrical resistivity, and κ is the thermal conductivity [4]. The coupled nature of the material proprieties encompassed by zT provides a challenge to obtaining high-efficiency thermoelectric materials.

Due to their complex crystal structures, tunable transport properties, and high temperature stability, Sb-based Zintl compounds such as $Yb_{14}MnSb_{11}$ ($zT \sim 1.4$ at 1200 K), Sr_3GaSb_3 ($zT \sim 0.9$ at 1000 K), Mg_3Sb_2 ($zT \sim 0.84$ at 773 K), $Ca_{1-x}RE_xAg_{1-y}Sb$ ($zT \sim 0.7$ at 1079 K), AM_2Sb_2 ($zT \sim 1.26$ at 700 K) and $Ca_5In_2Sb_6$ ($zT \sim 0.7$ at 1000 K) are promising candidates for use in thermoelectric applications

[5-10]. While the complex primitive cells of Zintl compounds reduce the velocity of the optical phonon modes, which lowers the lattice thermal conductivity [11], their covalently-bonded polyanionic structures may also contribute to the high electronic conductivity [4]. Through doping, these phases become extrinsic semiconductors with carrier concentrations in the range of 10^{19}-10^{21} carriers/cm^3 and exhibit significant improvements to their electronic properties and zT [12].

$Sr_5In_2Sb_6$, isostructural with $Ca_5In_2Sb_6$ [13], crystallizes in the $Ca_5Ga_2As_6$ (space group *Pbam*) structure type as reported by Cordier *et al.* [14] (Fig. 1). The crystal structure of $Sr_5In_2Sb_6$ consists of corner-linked chains of $InSb_4$ tetrahedra connected by Sb-Sb covalent bonds, forming ladder-like structures along the *c*-direction (described by: $[(4b)In^-]_2[(2b)Sb^-]_4[(1b)Sb^{2-}]_2$) and five ionically bonded Sr^{2+} atoms, which provide overall charge balance [8, 15]. The current study investigates the electronic and thermal transport properties of $Sr_5In_{2-x}Zn_xSb_6$ ($x = 0, 0.025, 0.05, 0.1$) and reports the enhanced thermoelectric performance that results from Zn-doping.
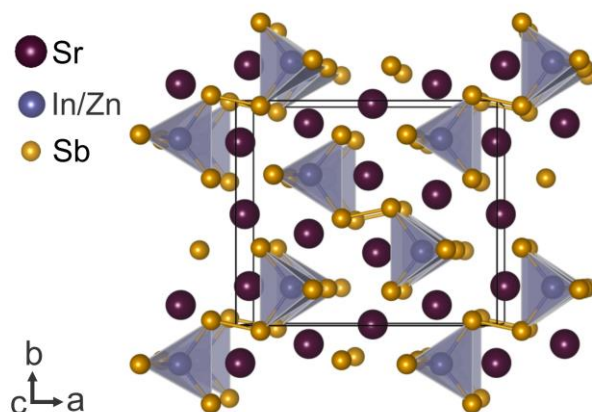

Figure 1: The crystal structure of $Sr_5In_{2-x}Zn_xSb_6$ contains corner-linked In(Zn)Sb$_4$ tetrahedra connected by Sb-Sb dimers to form double-chained ladders in the *c*-direction. Sr atoms are ionically bonded, providing overall charge balance.

Experimental Methods

The $Sr_5In_{2-x}Zn_xSb_6$ ($x = 0, 0.025, 0.05, 0.1$) series was synthesized using ball milling followed by hot pressing. An InSb precursor was prepared using stoichiometric amounts of In shot (99.999%, Alfa Aesar) and Sb shot (99.9999%, Alfa Aesar). The elements were vacuum sealed in double quartz ampoules and heated to 900 K at a rate of 150 K/h and annealed there for 12 h, then slowly cooled to room temperature. In an argon-filled glove box, stoichiometric quantities of InSb, Sb, dendritic Sr (99.9%, Sigma Aldrich), and Zn foil (99.99%, Alfa Aesar) were weighed and placed in a stainless-steel vial with two 0.5 inch diameter stainless-steel balls. The Sr was cut into 1-3 mm pieces before it was weighed. The samples were then ball milled using a high energy SPEX Sample Prep 8000 Series Mixer/Mill for one hour. Each resulting powder was loaded into a high-density graphite die (POCO) with a 12 mm inner diameter and hot pressed in an argon environment at 823 K for 2 hours under 110 MPa of pressure. The samples were then cut into ~ 1 mm thick disks.

X-ray diffraction (XRD) was performed using a Philips PANalytical XPERT MPD diffractometer with CuKα radiation in reflection mode. The crystal structure and the lattice parameters refinement using Si as internal standard were carried out by the WinCSD program package [16]. Scanning electron microscopy (SEM) and energy dispersive X-ray spectroscopy (EDS) were conducted using a Zeiss 1550 VP SEM to characterize the microstructure and to determine the phase purity. The chemical composition of the target phases was determined by electron probe micro-analysis (EPMA) with wavelength dispersive X-ray spectroscopy (WDS) using a JEOL JXA-8200 system. The Archimedes method was used to measure the sample densities. Hall effect and electrical resistivity measurements were performed using the Van der Pauw technique in a four-point probe setup with tungsten electrodes and a reversible 1 T magnetic field [17]. Seebeck measurements were carried out using W-Nb thermocouples and light-pipe heating –the temperature gradient across the samples were oscillated between ±10 K [18]. The electronic transport data was analyzed using solutions to the Boltzmann transport equation within the relaxation time approximation [19]. All electrical transport measurements were assumed to have ∼ 10 % error. The thermal diffusivity, D, was measured using the laser flash method with a Netzch LFA 457 instrument. The thermal conductivity, κ , was calculated using $\kappa = DC_pd$, where C_p is the Dulong-Petit approximation for heat capacity and d is the measured density of material. An error of approximately ∼ 5 % should be assumed for the thermal diffusivity. Room temperature optical measurements were performed using diffuse reflectance infrared Fourier transform spectroscopy (DRIFTS) [20]. A Thermo Scientific Nicolet 6700 FTIR spectrophotometer equipped with a Harrick Praying Mantis Diffuse Reflection accessory, DTGS detector and KBr beamsplitter was employed for the DRIFTS measurement. Raw reflectance data was used to estimate the absorption coefficient (scaled by the scattering coefficient) using the Kubelka Munk formula: $F(R) = \frac{(1-R)^2}{2R}$ [21]. Direct ($n = 2$) and indirect ($n = 1/2$) extrapolations of the absorption edge to the zero:$(F(R)\hbar\omega)^n \propto (\hbar\omega - E_g)$ were considered in order to estimate the transition onset energies [21, 22]. Because both extrapolations yielded reasonable fits, we used the calculated band structure to help us determine which interband transitions are likely responsible for the absorption edge features—as discussed in detail later in the text.

Results and Discussion

Chemical and Structural Characterization: $Sr_5In_{2-x}Zn_xSb_6$ samples were found to be air and moisture sensitive. X-ray diffraction patterns of the $Sr_5In_{2-x}Zn_xSb_6$ ($x = 0, 0.025, 0.05, 0.1$) samples showed no detectable secondary phase (see Fig. 2a). Lattice parameter refinement showed little change upon Zn substitution (see Table 1), which is expected as Zn and In have similar ionic radii (0.60 Å and 0.62 Å, respectively) [23]. The Rietveld refinement fit based on the reported structure model for the $Sr_5In_{1.9}Zn_{0.1}Sb_6$ sample is shown in Fig. 2b [14]. For that sample, all the Sr and the Sb positions were found to be fully occupied and the In site was found to be mixed occupied with Zn (Occ. In / Zn = 0.91(1) / 0.09(1)), corresponding to a refined composition of $Sr_5In_{1.82}Zn_{0.18}Sb_6$. This is in close agreement with the WDS result of $Sr_{4.94(2)}In_{1.818(6)}Zn_{0.195(5)}Sb_{6.05(2)}$. WDS results revealed a slight Sr deficiency and a slight In and Sb excess in the samples. In this work, the nominal compositions are used to refer to the samples. Microstructure analysis via SEM confirmed that the bulk materials were mostly phase pure with a < 1 wt.% Sb-excess secondary phase (Fig. 3). All samples were approximately 98-99 % of their theoretical density.
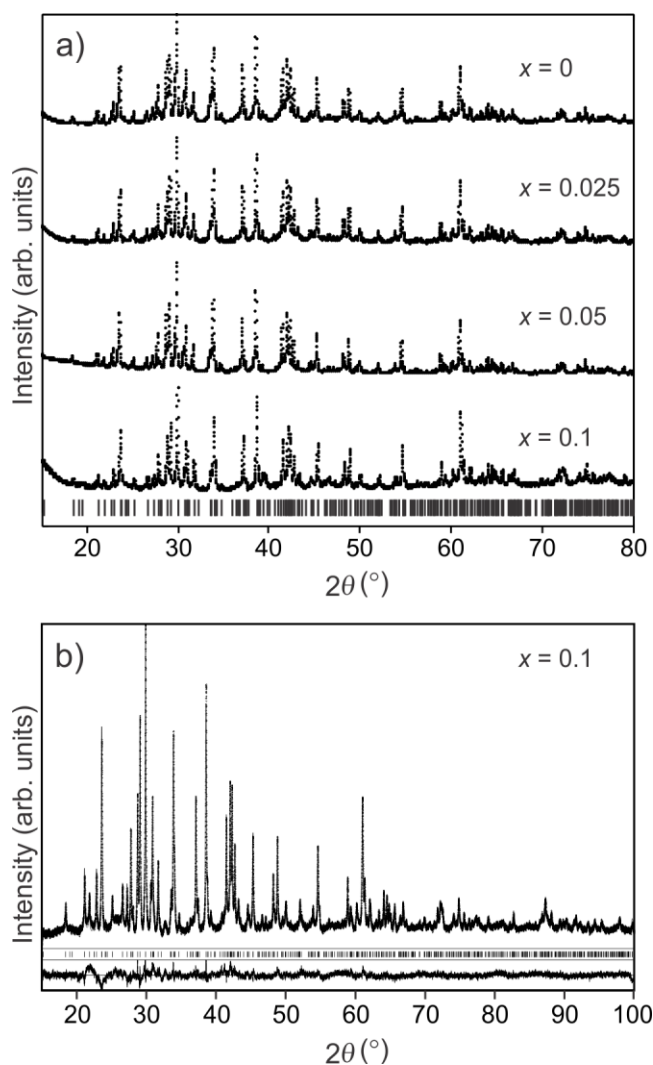
Figure 2: **a**) XRD (Cu-$K_{\alpha 1}$) patterns of the polycrystalline $Sr_5In_{2-x}Zn_xSb_6$ ($x = 0$, 0.025, 0.05, and 0.1) samples confirm the phase purities. **b**) The Rietveld fit of $Sr_5In_{1.9}Zn_{0.1}Sb_6$ based on the structure reported by Cordier *et.al* [14]. Almost all reflections can be indexed with the orthorhombic unit cell *Pbam* with lattice parameters shown in Table 1. The ticks mark the calculated reflection positions and the baseline corresponds to the residuals of the Rietveld refinement.

Table 1: Nominal and WDS compositions of $Sr_5In_{2-x}Zn_xSb_6$ ($x = 0$, 0.025, 0.05, 0.1) compounds and their corresponding lattice parameters.

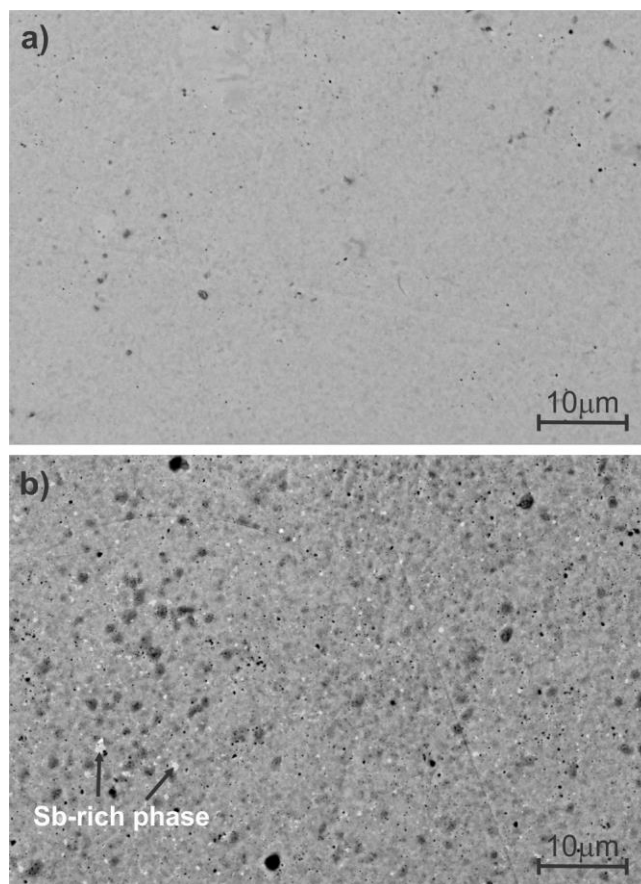| Nominal Comp.	WDS Compositions	Lattice Parameters (Å)
$Sr_5In_2Sb_6$	$Sr_{4.83(2)}In_{2.069(6)}Sb_{6.09(2)}$	$a = 14.768(2)$, $b = 12.700(2)$, $c = 4.6673(8)$
$Sr_5In_{1.975}Zn_{0.025}Sb_6$	$Sr_{4.85(2)}In_{2.031(6)}Zn_{0.021(5)}Sb_{6.10(2)}$	$a = 14.765(2)$, $b = 12.702(2)$, $c = 4.6668(7)$
$Sr_5In_{1.95}Zn_{0.05}Sb_6$	$Sr_{5.01(2)}In_{1.988(6)}Zn_{0.033(5)}Sb_{5.97(2)}$	$a = 14.773(2)$, $b = 12.709(2)$, $c = 4.6677(7)$
$Sr_5In_{1.9}Zn_{0.1}Sb_6$	$Sr_{4.94(2)}In_{1.818(6)}Zn_{0.195(5)}Sb_{6.05(2)}$	$a = 14.763(3)$, $b = 12.707(2)$, $c = 4.6666(7)$

Figure 3: SEM images of **a**) $x = 0.025$ and **b**) $x = 0.05$ samples in back-scattered electron mode. The former sample shows homogenous microstructure and the latter one contains small amounts of Sb-rich secondary phase which could not be identified by XRD analysis. Black spots are voids, while the dark grey spots are due to surface oxidation.

Electronic Transport Properties: Figure 4 shows the experimental carrier concentrations of the $Sr_5In_{2-x}Zn_xSb_6$ ($x = 0, 0.025, 0.05, 0.1$) series. The values are significantly lower than the predicted carrier concentration (dashed line) assuming each Zn leads to one free hole. This suggests that Zn does not fully replace In in the $Sr_5In_2Sb_6$ structure or that additional mechanisms (*e.g.* compensating site defects or impurities) are present [24, 25]. This contrasts with the nearly 100 % effective doping with Zn on the *M* site (*M* = Al, Ga, In) in $Ca_5M_{2-x}Zn_xSb_6$ compounds [8, 26, 27].
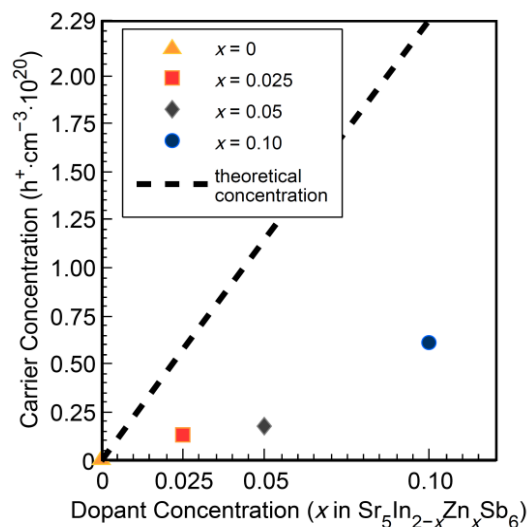
Figure 4: The Hall carrier concentration increases as a function of Zn concentration but deviates from the values predicted based on the assumption that each Zn atom contributes one carrier to the bulk material (dashed line).

The Hall carrier concentration, n_H, Hall mobility, μ_H, electronic resistivity, ρ, and Seebeck coefficients, α, are illustrated in Fig. 5. The carrier concentration increases with increasing dopant content and becomes increasingly temperature independent. A sample prepared with higher nominal Zn content, $x = 0.2$, did not lead to a higher carrier concentration. We suspect that the solubility limit of Zn in the $Sr_5In_2Sb_6$ matrix is reached somewhere near WDS composition for the $x = 0.1$ sample. All samples display poor mobilities (~ 2 - 3 cm^2/Vs at room temperature), which decrease further with increasing Zn concentration. Initially the mobility increases with increasing temperature, possibly due to ionized impurity scattering effects ($\mu \propto T^{3/2}$) [28] or a temperature activated process ($\mu \propto e^{-E_A/k_BT}$, E_A is the activation energy) [9] – the latter of which might be explained by impurity oxides or other secondary phases at the grain boundaries. Above 450 K for undoped and 550 K for Zn-doped samples, the mobility values start to decrease due to acoustic phonon scattering ($\mu \propto T^{-v}$, $1.0 \leq v \leq 1.5$) [9, 28]. There is a cusp in the $Sr_5In_2Sb_6$ mobility at 675 K, which is possibly attributed to a similar phase change seen in the isostructural $Ca_5M_2Sb_6$ systems (M = Al, In, Ga) [8, 29]. In the undoped $Sr_5In_2Sb_6$ sample, the temperature dependence of the resistivity points to non-degenerate semiconducting behavior. The resistivities of the doped

samples also decrease with temperature despite extrinsic doping, which can be explained by the positive temperature dependence of μ_H below 550 K. The Seebeck coefficients decrease with dopant concentration in line with a non-degenerate to degenerate semiconductor transition. At high temperatures n-type carrier activation is responsible for the decreasing Seebeck coefficients.
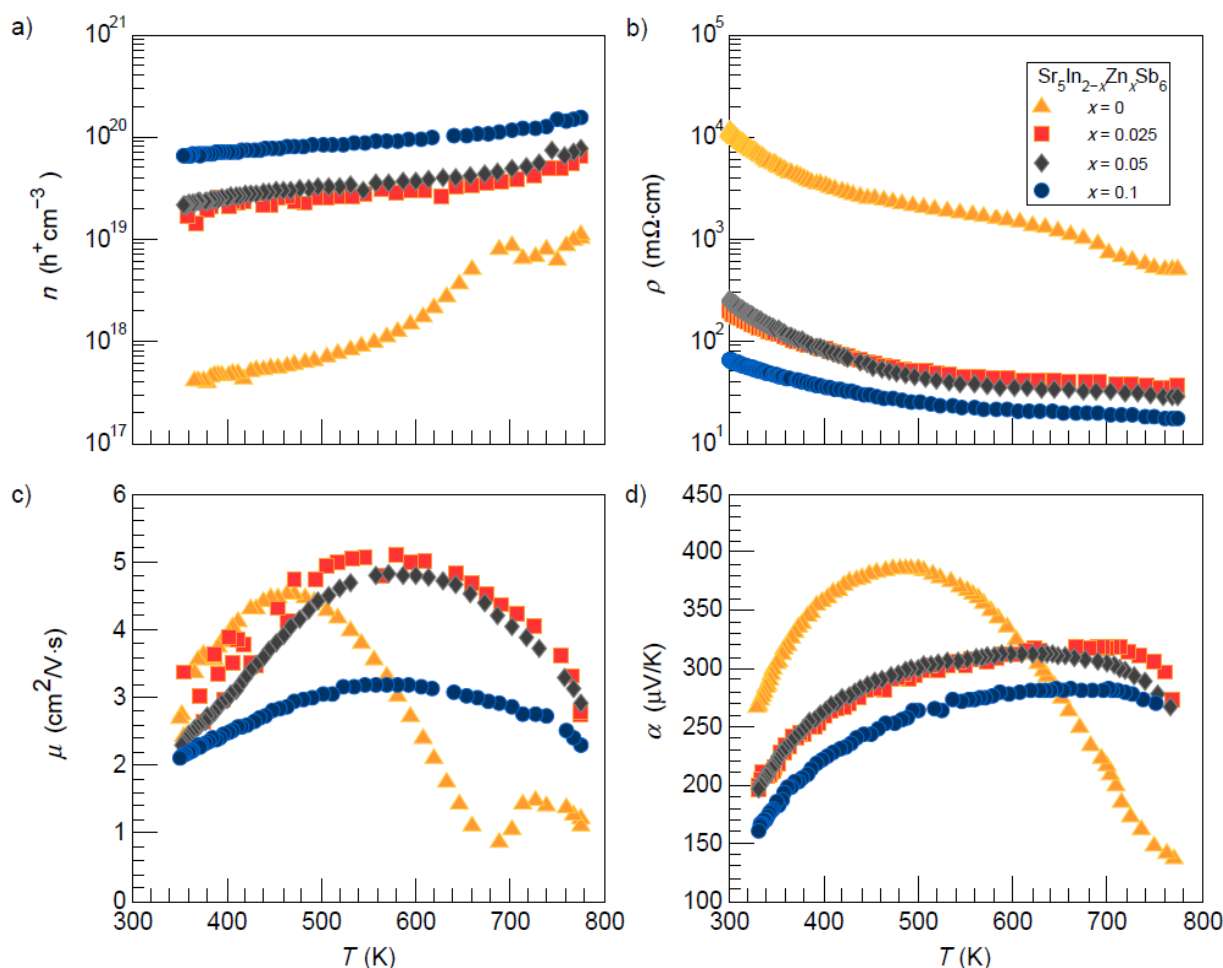
Figure 5: The temperature dependence of **a)** carrier concentration, **b)** resistivity, **c)** mobility and **d)** Seebeck coefficient for $Sr_5In_{2-x}Zn_xSb_6$ (x = 0, 0.025, 0.05, 0.1). Carrier concentrations increase and resistivity decreases with increasing Zn content. Mobilities are an activated process in this system at low temperatures.

Optical Measurements: Optical absorption results obtained using DRIFTS are shown in Fig. 6a for both $Sr_5In_2Sb_6$ from this work and $Ca_5In_2Sb_6$ from ref. [29] for comparison. In both systems, the optical absorption edge spectra show a slow rise for energies above ~ 0.3 eV followed by a faster rise above ~ 0.55 eV and ~ 0.65 eV for the $Sr_5In_2Sb_6$ and $Ca_5In_2Sb_6$ variants, respectively. By examining the calculated $Sr_5In_2Sb_6$ electronic band structure shown in Fig. 6b [13] we can examine which possible interband transitions might correspond to the features in the optical absorption edge spectrum. The interband transition with the lowest energy corresponds to the direct band gap near the X point with a calculated value of ~ 0.44 eV and 0.48 eV for $Sr_5In_2Sb_6$ and $Ca_5In_2Sb_6$ [13]. While the shallow rise at low energy in the optical data seems to indicate a weaker absorption feature (possibly an indirect gap or even mid-gap impurity states), we believe that this feature ($\hbar\omega_1$ as indicated in Fig. 6a and b) is due to the direct $X - X$ transition. As is commonly understood, direct gaps usually yield substantially higher optical absorption coefficients than indirect ones [30]; however, in this case the density of states for the lower-laying secondary valence bands at Γ is significantly higher (by about a factor of 10) than the band edge

states at X [13]. Optical measurements show that $\hbar\omega_1 \sim 0.3$ eV for both $Sr_5In_2Sb_6$ and $Ca_5In_2Sb_6$. The second increase in absorption ($\hbar\omega_2$) is possibly due to an indirect interband transition from one of several lower laying valence bands (the first of which is centered at the Γ point) to the conduction band edge. The extrapolation of the second absorption edge resulted in $\hbar\omega_2$ values of ~ 0.55 and 0.64 eV (see Fig. 6a) for $Sr_5In_2Sb_6$ and $Ca_5In_2Sb_6$ respectively, which differs from the true band gap by the phonon energy associated with the transition, $\hbar\Omega$. In comparison, DFT results for the $\Gamma - X$ transition energy are ~ 0.73 and 0.75 eV respectively, which show good agreement with the optical and theoretical results.

We can compare the optical results with other experimental estimations of the electronic band gap. The temperature dependent resistivity approximation of the band gap calculated from $\rho \propto e^{E_g/2k_BT}$ is ~ 0.26 eV at low temperatures and ~ 0.58 eV at high, which corroborates the optical absorbance data [31]. The Goldsmid-Sharp band gap estimated from the maximum Seebeck coefficient (~ 380 μV/K at 500 K for the undoped sample) using $E_g = 2e\alpha_{max}T_{max}$ is 0.38 eV [32]. Both estimates agree approximately with the optical and DFT results [33]. Additionally, it is well known that multiple-band effects can lead to excellent thermoelectric performance −as is the case in PbTe [34, 35]. However, for $A_5In_2Sb_6$ (A = Sr and Ca) the offset between the two bands is too large to improve the properties, requiring a chemical potential of ~ 0.25 eV to reach the second valence band which corresponds to a carrier concentration of ~ 10^{21} h$^+$/cm^3 (assuming single parabolic band at $T = 300$ K and $m^* = 1.3\ m_e$). Further investigation into whether the suggested offset is either a function of temperature or alloying, as in PbX (X = S, Se, Te) [34], can be performed to develop strategies towards band engineering in this system.

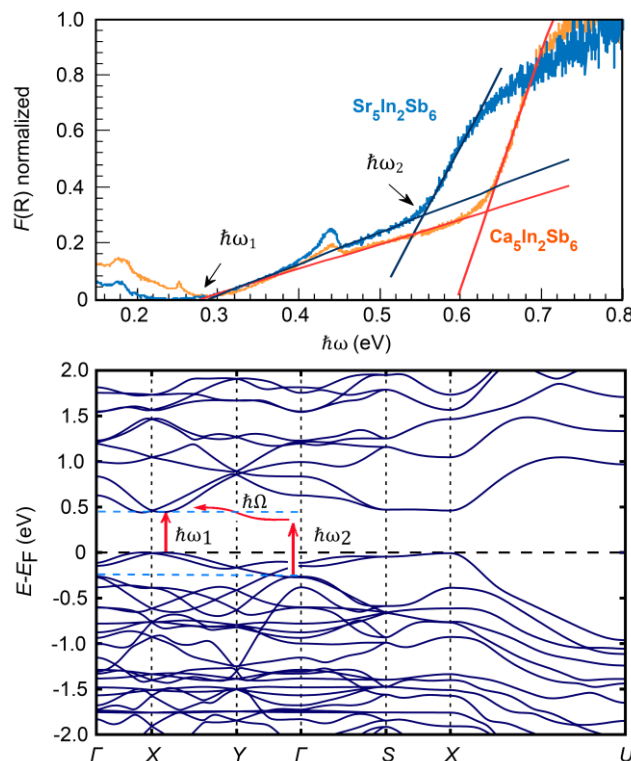**Figure 6**: **a**) Optical absorption edge results showing $F(R)$, the normalized Kubelka Munk function, for $Sr_5In_2Sb_6$ and $Ca_5In_2Sb_6$ where $\hbar\omega$ is the light energy in eV [21]. The two transitions at 0.3 eV and 0.55 eV are observed which are indicated by $\hbar\omega_n$ [36]. **b**) Calculated DFT band structure of $Sr_5In_2Sb_6$ with the suggested direct ($\hbar\omega_1 \sim 0.44$ eV) and indirect ($\hbar\omega_2 \sim 0.73$ eV) transitions indicated [13]. Both calculations indicate a difference of ~ 0.25 eV between the direct and indirect band gaps despite discrepancies in the band gap values.

Thermal Transport Properties: The total thermal conductivity, κ, of a material has contributions from phonons, which leads to lattice thermal conductivity (κ_L), and charge carriers, which give rise to the electronic thermal conductivity (κ_e) and bipolar thermal conductivity (κ_B) [4]. The total thermal conductivity increased slightly with increasing dopant concentration (Fig. 7a) due to the higher κ_e contributions. The electronic thermal conductivities were calculated using the Wiedemann-Franz law, $\kappa_e = LT\sigma$ (L is the Lorenz factor calculated from the single parabolic band (SPB) model as described in ref. [11]). The lattice and bipolar contribution to thermal conductivity ($\kappa_L + \kappa_B$) is shown in Fig. 7b. Overall, the electronic contribution to the thermal conductivity is minor. The samples show similar total and lattice thermal conductivities, but the bipolar effect is more pronounced for the undoped sample above 700 K. The $1/T$ decrease of κ as a function of temperature indicates that κ is limited by Umklapp scattering [8]. The minimum lattice thermal conductivity above the Debye temperature can be calculated from $\kappa_{min} = \frac{1}{2}\left(\frac{\pi}{6}\right)^{1/3} k_B V^{-2/3}(2v_T + v_L)$, where V is the average volume per atom and v_T and v_L are the experimental transverse and longitudinal sound velocities, respectively. The dashed line in Fig. 7b indicates the estimated κ_{min}

for $Sr_5In_2Sb_6$ with $v_T = 2120$ m/s and $v_L = 3580$ m/s [13]. The κ_L values of all samples are found to be higher than $\kappa_{min} = 0.42$ W/mK suggesting a further reduction to κ_L is possible.
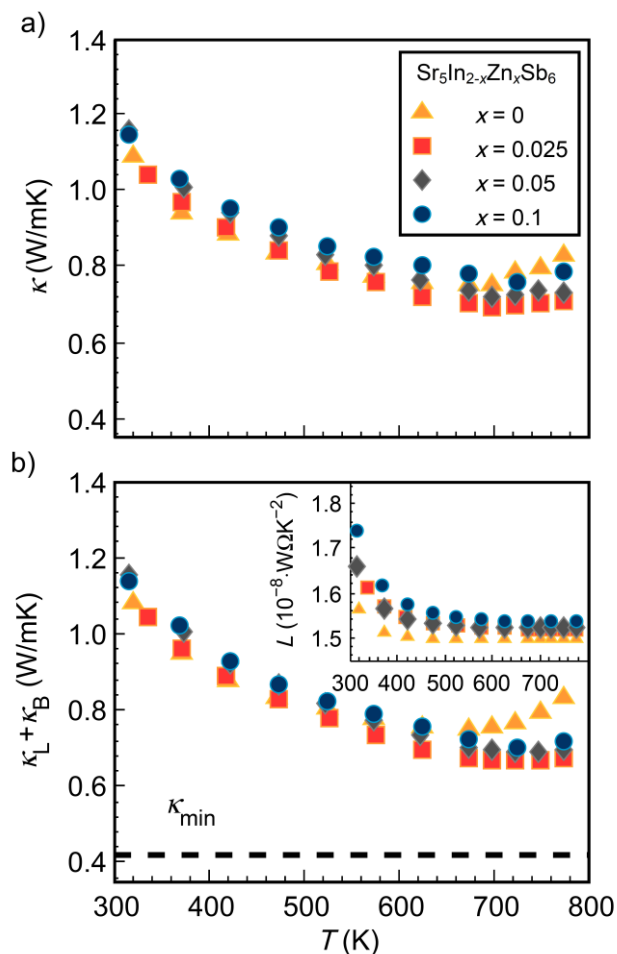

Figure 7: The temperature dependence of the **a)** κ and **b)** $\kappa_L + \kappa_B$, with the Lorenz factors used to calculate κ_e shown in the inset. The thermal conductivity is dominated by the lattice contribution.

Thermoelectric Figure of Merit: The figure of merit, zT, is shown as a function of temperature in Fig. 8a. The zT values increase with increasing doping concentration, reaching values slightly lower than that of Zn-doped $Ca_5In_2Sb_6$ at 750 K. However, due to the smaller band gap and thus earlier onset of minority carrier activation, and lack of dopant activation, the peak zT in Zn-doped $Sr_5In_2Sb_6$ (~ 0.4 at 700 K) is lower and occurs at lower temperatures than the peak zT of the Ca analogue (~ 0.7 at 950 K) [8].

The poor mobility in the $Sr_5In_{2-x}Zn_xSb_6$ system also has an overall negative impact on the electronic transport properties. An analysis of the experimental data using a single parabolic band (SPB) model at 350 K and 500 K assuming an effective mass, m^*_{SPB}, of 1.3 m_e and 2.2 m_e, an intrinsic mobility, μ_o, of 4.05 and 4.8 cm²/V·s, and κ_L of 1.0 and 0.8 W/m·K, respectively, is illustrated in Fig. 9. At 350 K, m^*_{SPB} for $Sr_5In_2Sb_6$ is similar to the density of states (DOS) effective mass reported in ref. [13] ($m^*_{DOS} = 1.13 \, m_e$). Compared with Zn-doped $Ca_5In_2Sb_6$, m^*_{SPB} in Zn-doped $Sr_5In_2Sb_6$ is

smaller at room temperature (as predicted in ref. [13]), but the effective masses become nearly identical above 500 K. The peak zT predicted in this model occurs at a carrier concentration above 10^{20} h$^+$/cm^3, suggesting that a further increase in carrier concentration is necessary to optimize zT in Sr$_5$In$_2$Sb$_6$.
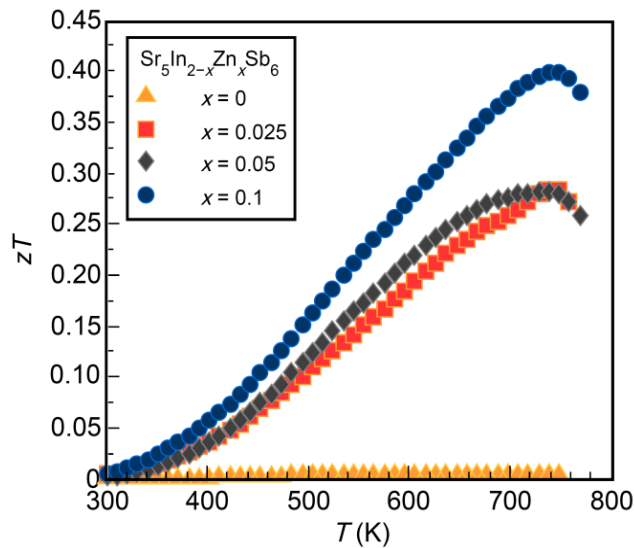

Figure 8: **a)** The thermoelectric figure of merit as a function of temperature shows the zT enhancement by Zn doping. A zT of ~ 0.4 at around 750 K is reached in the most heavily doped sample.
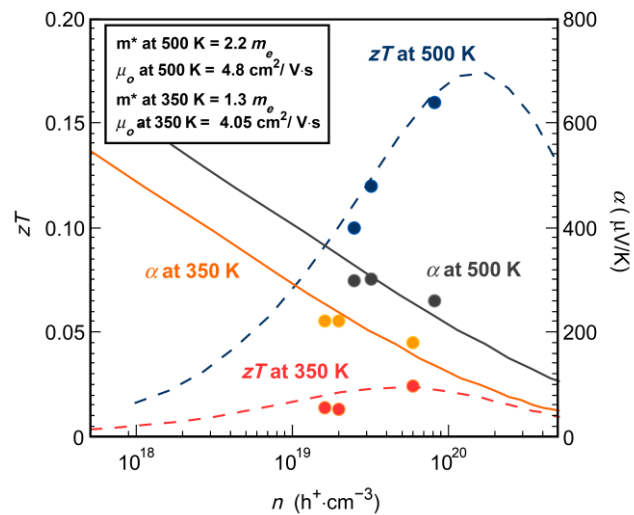

Figure 9: The solid and dashed curves are the SPB model α and zT values, respectively, as a function of n. The experimental zT values are still lower than the optimum amount predicted by the model, suggesting further optimization is possible.

Conclusion

Zn-doped $Sr_5In_2Sb_6$ was successfully synthesized via ball milling followed by hot pressing processes. The electronic transport properties of the samples show a transition from non-degenerate to degenerate semiconducting behavior with increasing Zn content. Despite the complex band structure of $Sr_5In_2Sb_6$, the figure of merit as a function of carrier concentration can be described using a single parabolic band model. Optical absorption measurements and the calculated band structure revealed two distinct energy transitions with energies of ~ 0.3 eV and ~ 0.55 eV, respectively: one from the valence edge to the conduction band and another from a lower valence band manifold to the conduction band. The lattice thermal conductivity - the main contributor to κ - had a minimum of ~ 0.7 W/mK at 700 K, suggesting there is potential to further lower κ by ~ 0.3 W/mK. A peak zT of 0.4 was achieved at around 750 K in the most heavily Zn-doped sample; however, the SPB model suggests further doping is required for optimization. With improved processing techniques to increase the carrier concentration and mobility, a higher figure of merit can potentially be achieved.

References

1. Bell, L.E., *Cooling, Heating, Generating Power, and Recovering Waste Heat with Thermoelectric Systems*. Science, 2008. **321**: p. 1457.
2. DiSalvo, F.J., *Thermoelectric Cooling and Power Generation*. Science, 1999. **285**: p. 703-706.
3. Nolas, G.S., J. Sharp, and H.J. Goldsmid, *Thermoelectrics- Basic Principles and New Materials Developments*. 2001, Germany: Springer, Heidelberg.
4. Snyder, G.J. and E.S. Toberer, *Complex Thermoelectric Materials*. Nature Mater, 2008. **7**: p. 105-114.
5. Wang, J., et al., *Ca1-xRExAg1-ySb (RE = La, Ce, Pr, Nd, Sm; 0 <= x <= 1; 0 <= y <= 1): Interesting Structural Transformation and Enhanced High-Temperature Thermoelectric Performance*. Journal of the American Chemical Society, 2013. **135**(32): p. 11840-11848.
6. Guo, K., Q.G. Cao, and J.T. Zhao, *Zintl phase compounds AM(2)Sb(2) (A=Ca, Sr, Ba, Eu, Yb; M=Zn, Cd) and their substitution variants: a class of potential thermoelectric materials*. Journal of Rare Earths, 2013. **31**(11): p. 1029-1038.
7. Bhardwaj, A. and D.K. Misra, *Enhancing thermoelectric properties of a p-type Mg3Sb2- based Zintl phase compound by Pb substitution in the anionic framework*. Rsc Advances, 2014. **4**(65): p. 34552-34560.

8. Zevalkink, A., J. Swallow, and G.J. Snyder, *Thermoelectric properties of Zn-doped Ca5In2Sb6*. Dalton Trans., 2013. **42**: p. 9713-9719.

9. Zevalkink, A., et al., *Thermoelectric properties of Sr3GaSb3 – a chain-forming Zintl compound.* Energy Environ. Sci., 2012. **5**: p. 9121-9128.

10. Brown, S.R., et al., *Yb14MnSb11: New High Efficiency Thermoelectric Material for Power Generation.* Chemistry of Materials, 2006. **18**(7): p. 1873-1877.

11. Ohno, S., et al., *Thermoelectric properties of the Yb9Mn4.2−xZnxSb9 solid solutions.* Journal of Materials Chemistry A, 2014. **2**(20): p. 7478.

12. Toberer, E.S., A.F. May, and G.J. Snyder, *Zintl Chemistry for Designing High Efficiency Thermoelectric Materials.* Chemistry of Materials, 2010. **22**(3): p. 624-634.

13. Zevalkink, A., et al., *Thermoelectric properties and electronic structure of the Zintl phase Sr5In2Sb6 and solid solution Ca5-xSrxIn2Sb6.* Journal of Physics: Condensed Matter, 2015. **27**(1).

14. Cordier, G., H. Schäfer, and M. Stelter, Z. Naturforsch. b, 1985. **40**: p. 5-8.

15. Kauzlarich, S.M., ed. *Chemistry, Structure, and Bonding of Zintl Phases and Ions.* 1996, VCH Publishers Inc.: New York.

16. Akselrud, L. and Y. Grin, *WinCSD: software package for crystallographic calculations (Version 4).* Journal of Applied Crystallography 2014. **47**: p. 803-805.

17. Borup, K.A., et al., *Measurement of the electrical resistivity and Hall coefficient at high temperatures.* Review of Scientific Instruments, 2012. **83**(12): p. 123902.

18. Wood, C., D. Zoltan, and G. Stapfer, *Measurement of Seebeck coefficient using a light pulse.* Review of Scientific Instruments, 1985. **56**(5): p. 719-722.

19. May, A., et al., *Characterization and analysis of thermoelectric transport in n-type Ba8Ga16−xGe30+x.* Physical Review B, 2009. **80**(12): p. 125205.

20. Zachary, M.G., L. Aaron, and G.J. Snyder, *Optical band gap and the Burstein–Moss effect in iodine doped PbTe using diffuse reflectance infrared Fourier transform spectroscopy.* New Journal of Physics, 2013. **15**(7): p. 075020.

21. Kubelka, P. and F. Munk, *Reflection characteristics of paints.* Z. Technische Physik, 1932. **12**: p. 593-601.

22. Basu, P.K., *Theory of Optical Processes in Semiconductors.* Series on Semiconductor Science and Technology. 1997: Oxford University Press.

23. Shannon, R.D. and C.T. Prewitt, *Revised values of effective ionic radii.* Acta Cryst., 1970. **B26**: p. 1046.

24. Zunger, A., *Practical doping principles.* Applied Physics Letters, 2003. **83**(1): p. 57-59.

25. Zevalkink, A., *Chain-Forming Zintl Antimonides as Novel Thermoelectric Materials*, in *Applied Physics and Materials Science.* 2013, California Institute of Technology: Pasadena.

26. Toberer, E.S., et al., *The Zintl Compound Ca5Al2Sb6 for Low-Cost Thermoelectric Power Generation.* Advanced Functional Materials, 2010. **20**(24): p. 4375-4380.

27. Johnson, S.I., A. Zevalkink, and G.J. Snyder, *Improved thermoelectric properties in Zn-doped Ca5Ga2Sb6.* Journal of Materials Chemistry A, 2013. **1**(13): p. 4244-4249.

28. Amith, A., I. Kudman, and E.F. Steigmeier, *Electron and Phonon Scattering in GaAs at High Temperatures.* Physical Review, 1965. **138**(4A): p. A1270-A1276.

29. Zevalkink, A., et al., *Influence of the Triel Elements (M = Al, Ga, In) on the Transport Properties of Ca5M2Sb6 Zintl Compounds.* Chemistry of Materials, 2012. **24**(11): p. 2091-2098.

30. Gnutzmann, U. and K. Clausecker, *Theory of direct optical transitions in an optical indirect semiconductor with a superlattice structure.* Applied Physics 1974. **3**(1): p. 9-14.

31. Simonson, J.W. and S.J. Poon, *Electronic structure of transition metal-doped XNiSn and XCoSb (X = Hf,Zr) phases in the vicinity of the band gap.* Journal of Physics: Condensed Matter, 2008. **20**(25): p. 255220.

32.   Gibbs, Z.M., et al., *Band gap estimation from temperature dependent Seebeck measurement—Deviations from the 2e|S|maxTmax relation.* Applied Physics Letters, 2015. **106**(2): p. 022112.

33.   Schmitt, J., et al., *Resolving the true band gap of ZrNiSn half-Heusler thermoelectric materials.* Mater. Horiz., 2014. **2**(1): p. 68-75.

34.   Gibbs, Z.M., et al., *Temperature dependent band gap in PbX (X = S, Se, Te).* Applied Physics Letters, 2013. **103**(26): p. 262109.

35.   Pei, Y., et al., *Convergence of electronic bands for high performance bulk thermoelectrics.* Nature, 2011. **473**(7345): p. 66-9.

36.   Tauc, J., *Optical properties and electronic structure of amorphous Ge and Si.* Materials Research Bulletin, 1968. **3**(1): p. 37-46.